International Journal of Disaster Risk Reduction 142 (2026) 106224

Contents lists available at ScienceDirect

International Journal of Disaster Risk Reduction

journal homepage: www.elsevier.com/locate/ijdrr

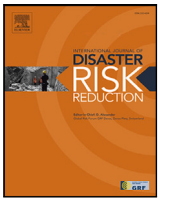

Multi-hazards assessment in Türkiye following large earthquakes

E. Mills [a,*], R. Chahel [a], H. Hourston [a], A. Winson [a], M.B. Sørensen [c], L. Lombardo [b], E. Hussain [a], B. Van den Bout [b], H. Tanyas [b], A. Novellino [a]

[a] British Geological Survey, Keyworth, Nottingham, NG12 5GG, United Kingdom
[b] University of Twente, Faculty of Geo-Information Science and Earth Observation (ITC), PO Box 217, Enschede, AE 7500, Netherlands
[c] Department of Earth Science, University of Bergen, Bergen 5020, Norway

ARTICLE INFO

Keywords:
Türkiye
Multi-hazard susceptibility
Earthquake
Co-seismic landslide
Floods

ABSTRACT

The Mw 7.8 and Mw 7.5 Kahramanmaraş Earthquake Sequence (KES) of 6th of February 2023 generated one of the most complex multi-hazard disasters in modern Türkiye, triggering thousands of landslides, severe liquefaction, widespread infrastructure damage, and subsequent flooding enhanced by an atmospheric river event. While these cascading impacts highlighted the tight coupling between seismic, geomorphic and hydrometeorological processes, quantitative multi-hazard assessments for the region remain limited. In this study, we develop an integrated, scenario-based framework to evaluate future spatially compounding hazards in southeastern Türkiye over a 50-year horizon. Earthquake ground shaking is modelled using six deterministic rupture scenarios based on seismic gaps along the East Anatolian Fault Zone. These shaking fields have then been ingested into a Generalised Additive Model (GAM) with Bayesian (Integrated Nested Laplace Approximation) INLA estimation to map co-seismic landslide susceptibility across 540,000 slope units using terrain metrics, lithology, InSAR-derived pre- and post-event deformation, and PGA. Flood hazards are simulated using the FastFlood model, incorporating design storms derived from IDF-Space statistics, CMIP6-based climate projections, soil and landcover datasets and river discharge. Landslide and flood layers are spatially harmonised and combined using the TOMRAP tool to produce a regional multi-hazard susceptibility map.

Results show persistent hazard hotspots where steep terrain, susceptible lithologies, and strong shaking overlap with fluvial corridors, particularly along the northern and central sectors of the study area. The 50-year flood scenario indicates widespread inundation in major valleys, with local depths exceeding 20 m in confined reaches. When combined, multi-hazard susceptibility reaches its highest levels along mountain fronts, valley margins, and areas repeatedly exposed to both strong ground motions and hydrodynamic flooding. Exposure analysis reveals that approximately 702,000 buildings and 5.0 million people fall within mapped hazard classes, including more than 118 buildings and 850 residents in the highest hazard category. Our findings demonstrate the critical role of earthquake legacy effects, hillslope preconditioning, and hydrological amplification in shaping future multi-hazard occurrence.

* Corresponding author.
E-mail address: e.mills@bgs.ac.uk (E. Mills).

https://doi.org/10.1016/j.ijdrr.2026.106224
Received 10 March 2026; Received in revised form 22 May 2026; Accepted 23 May 2026

Available online 2 June 2026

1. Introduction

Large earthquakes are among the most destructive natural hazards, with impacts that extend beyond the immediate seismic shaking [1]. In addition to causing direct structural damage and loss of life, strong ground motions can significantly alter geomorphic processes, particularly those related to slope stability and hydrological dynamics. Earthquakes can weaken hillslope materials, trigger landslides [2], and modify surface and subsurface conditions in ways that increase susceptibility to flooding e.g., landslide dams [3]. These cascading and compounding effects often persist for months or even years after the initial seismic event, contributing to the post-seismic legacy effect [1,4]. Despite the growing recognition of these interactions, studies that systematically assess multi-hazard processes, especially those combining earthquakes, landslides, and floods, remain limited [5]. Most hazard assessments treat these phenomena in isolation, overlooking the complex interactions and spatial dependencies that can amplify risk in vulnerable regions. This gap is particularly critical in tectonically active areas, where the interplay between seismic activity, slope instability and hydrological extremes can lead to devastating outcomes.

In this study, we present a novel approach to assess long-term compounding hazards in southeastern Türkiye, a region that experienced the catastrophic Mw 7.8 and Mw 7.5 Kahramanmaraş earthquake sequence (KES) in February 2023. Türkiye is characterised by high geological risk, with frequent and well-documented occurrences of earthquakes [6], landslides [7] and floods [8]. The East Anatolian Fault Zone (EAFZ), which ruptured during the 2023 sequence, crosses mountainous terrain with steep slopes and variable lithology, creating ideal conditions for multi-hazard interactions [9]. What makes this event particularly unique is the unprecedented availability of both satellite and ground-based observations, in addition to grey literature sources documenting the event and its aftermath. These rich datasets enable the identification of spatial relationships between different hazards, offering a rare opportunity to build comprehensive models that capture the compounding effects of seismic activity on slope stability and flood dynamics.

To quantify these interactions, we developed a scenario-based compound hazard perspective, focusing on how independently modelled hazards may spatially and temporally co-occur under plausible future conditions. The approach combines statistical and physical modelling. We first derived earthquake ground shaking scenarios based on ground motion models (GMM). These scenarios were used to simulate co-seismic landslide hazards using a Generalised Additive Model (GAM), which captures non-linear relationships with the predictors. We then assessed flood hazards in terms of extension and depth using a physically-based steady-state flow model FastFloods [10]. Finally, we combined landslide hazard with flood hazard using the Tool for Multi-Risk Assessment in Python – TOMRAP tool [11] and produced a comprehensive multi-hazard susceptibility assessment.

To note, we do not model dynamically coupled multi-hazard processes (e.g., landslide-altered hydrology or sediment-driven flood amplification). Instead, we adopt a spatial co-occurrence framework in which earthquake-triggered landslide susceptibility and a 1-in-50-year flood hazard are modelled independently using the most appropriate methods for each process. Earthquakes and landslides are treated as a triggering (cascading) pair, whereas flooding is incorporated as a compound hazard that may spatially coincide with earthquake-affected terrain within the planning horizon. The resulting multi-hazard product therefore represents areas of potential co-occurrence rather than dynamically interacting hazards.

By leveraging statistical modelling and remote sensing data, this paper aims to offer a scalable and transferable methodology for assessing compound hazards in seismically active regions. The results not only highlight the spatial and temporal evolution of multiple hazards following major earthquakes but also underscore the importance of multi-hazard frameworks in disaster risk reduction and resilience planning.

2. Study area

The southeastern region of Türkiye has a history of large, damaging natural hazards, most notably earthquakes, floods and landslides. Our study focuses on a region of approx. 70,000 km^2 heavily affected by the February 6, 2023, earthquake sequence (Fig. 1). The area enclosed by the 0.12 g peak ground acceleration (PGA) isoline was previously surveyed for co-seismic landslides [12]. Within this area there are approx. 2.3M buildings, according to the Global Building Atlas dataset [13], and 9.7M people, according to the WorldPop database for the year 2020.

The study area is situated along the East Anatolian Fault (EAF), a major intracontinental left-lateral strike-slip fault zone that accommodates the relative motion between the Anatolian and Arabian plates [14]. The EAF extends from the Karlıova triple junction in the northeast, where it intersects the North Anatolian Fault (NAF), to the Iskenderun Gulf in the southwest, spanning approximately 550 to 700 km in length [15,16]. Together the NAF and EAF facilitate the westward motion of Anatolia towards the Hellenic subduction zone [17,18]. The EAF fault system comprises over 15 segments, with slip rates ranging from approximately 11 mm/yr in the north to around 4.5 mm/yr in the south [19–21].

In the early hours of 6 February 2023, a magnitude 7.8 earthquake struck the Kahramanmaraş region of south-eastern Türkiye. The first quake was followed by a magnitude 6.7 initial aftershock just eleven minutes later. Nine hours later, a magnitude 7.6 earthquake also shook the region, approximately 90 km northeast. The relatively shallow focal depth of the surface-rupturing earthquakes resulted in strong–violent shaking (Modified Mercalli Intensity 6–9) and impacted vulnerable communities over a large area of southeast Türkiye and northern Syria [22].

KES claimed over 50,000 lives across 11 provinces, with more than 9 million people affected. An estimated 37,000 buildings collapsed, an additional 230,000 were heavily damaged across Türkiye, and over 10,600 across the border in nearby Syria [23]. As a result, approximately 3.6 million people were left without homes to safely reside within an area of 90,000 km^2, a similar sized area to the country of Portugal [24]. With over 50,000 aftershocks recorded in the 9 months post-event [25], there were significant

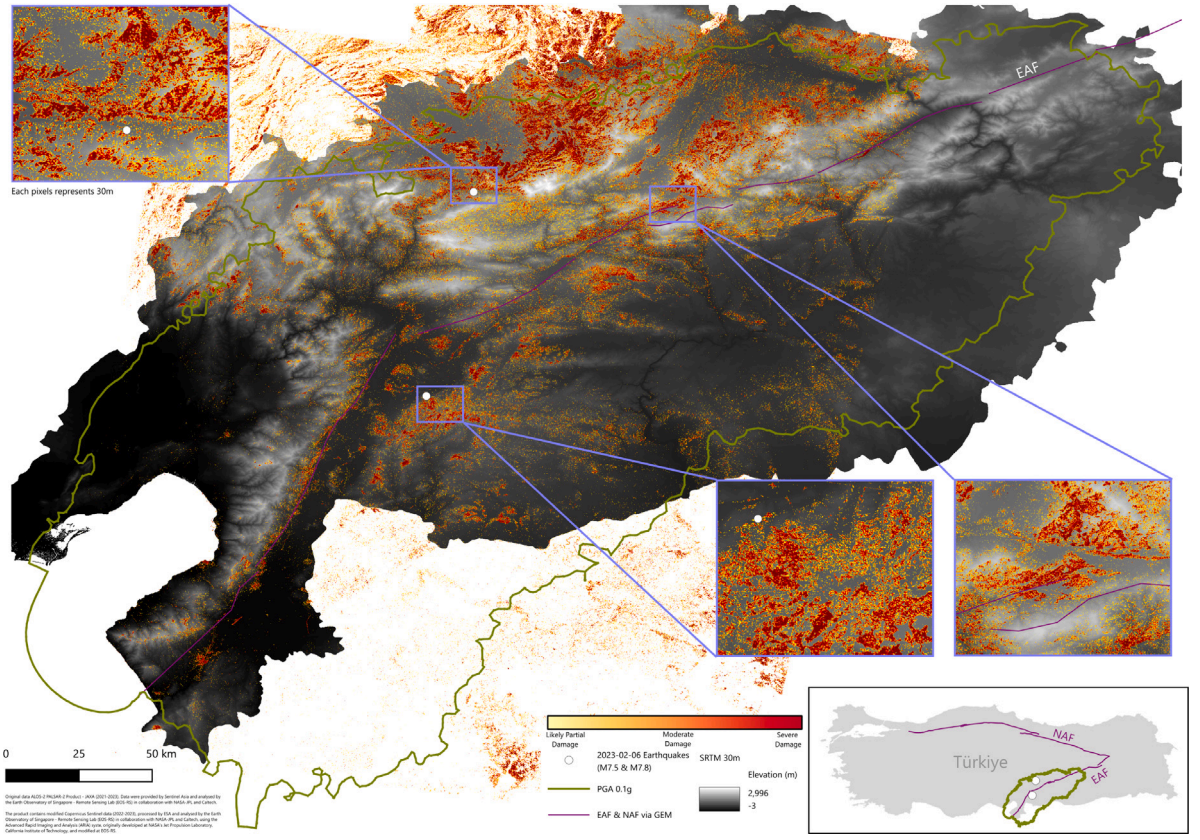

Fig. 1. Map highlighting the damage proxy dataset for the Kahramanmaraş earthquake sequence produced by EOS (Earth Observatory of Singapore) in partnership with NASA. Moving from yellow to red colours is associated with a high probability of damage. Image modified from: https://storymaps.arcgis.com/stories/079f097d5499466385736792e09b31f3. In the subset, location of the study area and main faults.

difficulties conducting damage assessments and rescue operations in addition to the delivery of aid and resources in the immediate aftermath. This was hindered further by the estimated 100 cubic meters of rubble and debris that had to be cleared from high-traffic areas across southeastern Türkiye [26].

Major deformation extended approximately 350 and 150 km along the southern and northern strands bifurcating in the west of the East Anatolian Fault, produced by the main shock and the largest aftershock [27]. As a direct result of the KES, more than 3600 co-seismic landslides were mapped, mainly concentrated in the northern sections of the most impacted area [12], followed by further landslides triggered by an atmospheric river — which hit the same region a month later [9]. Yet this does not consider the long-term impacts of intense seismic shaking on almost 400 slope instabilities that were either accelerated or decelerated by the KES [28].

The landslides experienced exacerbated the flooding hazard of the area, in conjunction to the extreme hydrometeorological conditions at the onset of the event. Intense rainfall and resultant flooding hit the cities of Adıyaman Şanlıurfa and Çelikhan [29]. This compounding cascade of hazards highlights the need to better integrate seismic and hydrometeorological extremes into rapid hazard assessment protocols, to enhance disaster preparedness and timely response.

Further, the complex multi-hazard interactions and associated impacts of the multifaceted event were captured in an internal Hazard Impact Catalogue (HIC) utilising various sources ranging from humanitarian response logs, news and media reportings, and high-level government/NGO reporting. On-the-ground impacts could be identified and recorded in near-real time [30] and used to form the basis of the subsequent impact chain (see Fig. 2). Impact Chains are common conceptual or data-driven tools used in climate risk-vulnerability studies [30,31], capturing the most relevant factors contributing to a specific risk [32]. Collating these hazards and associated impact sources allows the complexity of the KES event to be captured and logged in the HIC and visualised in an impact chain, and to gauge temporal sequencing of the primary and secondary hazards, and their mechanisms. The impact chain presented is not intended to represent the structure of the numerical modelling framework implemented in this study — as not all interactions can be explicitly modelled, but it provides contextual justification for considering earthquakes, landslides and flooding with a unified multi-hazard assessment.

Within the HIC, available literature and published inventories, several distinct compound hazard classes were identified — with each class containing a large volume of individual events interactions. Within the earthquake-landslide compound class, over 3500

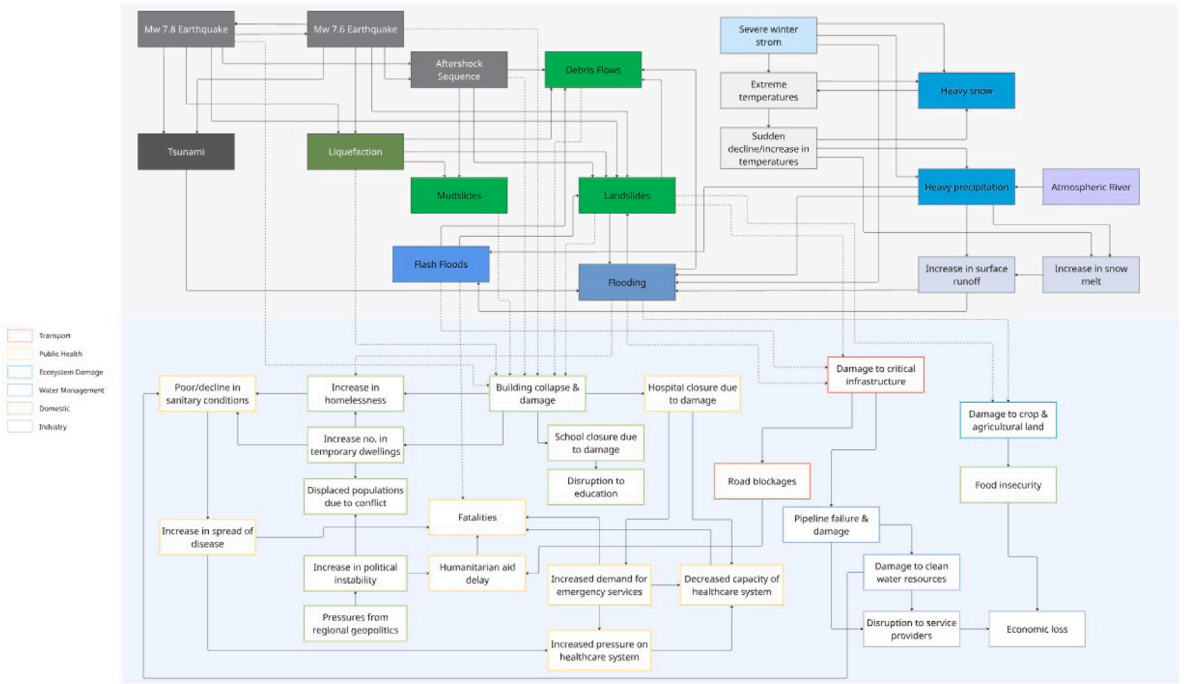

Fig. 2. Impact chain derived from the HIC, highlighting the hazard interactions and subsequent impacts from the earthquake sequence.

events were noted, yet there are discrepancies across sources. A small number of compound landslide-flood events were recorded in relation to sediment damming water bodies and rivers. Remobilised slopes through earthquake legacy effects compounding with a hydro-meteorological trigger occurred, with 10 significant debris flows reported [33]. Earthquake-liquefaction compounds were reported, but this is difficult to quantify; over 1800 individual sites were mapped using post-event imagery [34], noting the occurrence of mass structural failure and coastal subsidence-related inundation [35]. The compound of earthquake–submarine landslide resulted in a small Mediterranean tsunami [36], while the entire event sequence was driven by the earthquake compound of the first event altering the stress conditions that resulted in the second.

It is important to note that the trigger of these hazards may differ between events reported, but the associated impacts across events, and in turn hazards more broadly, are similar in nature. Damage to critical infrastructure, buildings and agricultural land was extensively recorded across all hazard types in the KES, with poor enforcements of building regulations and in turn increased shaking being a key driver of damage [37]. Aid and response were delayed due to the affected road network in and around dense urban areas and heightened political instability [22]. Those impacted by ground shaking were met with winter storm conditions, extreme precipitation and intense aftershocks in the event's immediate aftermath.

The impact chain highlights the complexity of the event's spatio-temporal hazards and associated impacts which had a wider social and economic cost. One hazard rarely occurs in isolation, providing context to the modelling approach of co-seismic landslides and floods. The hazard landscape of Türkiye, the 2023 events pre-conditioning and the accumulation of events highlights the importance of understanding the spatio-temporal interrelationships of hazards and how they can be assessed.

3. Datasets and methodology

Our multi-hazards analysis includes the assessment of earthquake-triggered landslides and flood hazards. The inputs datasets span geomorphological, seismic, hydrological and demographic domains (Table 1) which we describe in detail across the next subchapters.

Following Tilloy et al. [38], we distinguish between triggering (cascading) interactions and compound hazards. In our framework, earthquakes act as the primary trigger for co-seismic landslides, which are explicitly modelled using a statistical GAM-INLA approach. Flooding, by contrast, is treated as a compound hazard that is not causally linked to the earthquake scenarios but may spatially overlap with landslide-susceptible terrain within the 50-year horizon. The multi-hazard susceptibility map therefore combines: (i) earthquake-triggered landslide susceptibility, and (ii) probabilistic flood hazard, using a harmonised indexing scheme.

To summarise;

- **Triggering** (Cascading), whereby earthquakes act as the primary event and directly trigger secondary hazards. This relationship is explicitly modelled through the generation of earthquake-triggered landslide susceptibility maps for a set of deterministic seismic scenarios.

Table 1
Main datasets used throughout this methodology. More details about each is provided in the text.

Dataset	Year	Original resolution or scale	Source
DTM	2019	5 m	AFAD and Turkish Command of Mapping
Sentinel-1	Feb2020–Feb2024	5 × 20 m	European Space Agency
Sentinel-2	Sep2022–Feb2023 (pre-event); Apr2023–Jul2023 (post-event)	10 m	European Space Agency
Geology	1991–2004	1:100,000 scale	General Directorate of Mineral Research and Exploration (MTA, 1998)
Global Flood Database			GFD
Global Surface Water Explorer			GSWE
Land Cover	2019	10–100 m	Copernicus Global Land Cover Layers, European Space Agency
Lithology	1998	1:100,000 scale	
Peak Ground Acceleration	2023–2050	1000–10,000 m	Ground Motion Model (GMM)
Precipitation	Every 30 mins	approx 10,000 m	GPM IMERG
Soil Properties	2020	250 m	SoilGrids 2.0
Urban Infrastructure and Flood Protection	2025	N/A	OpenStreetMaps via Global Building Atlas

- **Compound**, where multiple hazards are considered together based on their spatial concurrence within a common planning horizon, rather than through a direct causal linkage. In this study, flood hazard is combined with the earthquake-triggered landslide susceptibility maps as a compounding hazard, with the two processes treated as conditionally independent and not modelled as a direct cascade.

We detail how these hazards maps have been created in terms of input files and approach for each phenomenon: earthquakes (Section 3.1), landslides (Section 3.2) and floods (Section 3.3). In Section 3.4 we detail how we combined the individual hazards maps into a multi-hazards map into a simpler yet equally effective GIS overlay scheme. The final multi-hazard product represents areas where earthquake-triggered landslide susceptibility and flood hazard may co-occur spatially, rather than simulating dynamically coupled interactions or feedbacks between seismic, geomorphic and hydrological processes. A return period of 50-years was selected because longer time horizons provide more robust climate projections, which are essential for accurately assessing flood hazards.

In order to estimate a proper likelihood of two hazards to occur simultaneously or at least with some degree of reciprocal influence, statistics demands the implementation of a joint modelling architecture [39–41]. However, this is typically done when two hazards or two parameters are both modelled in a data-driven manner. In our case, we modelled each respective hazard with the most suitable and scientifically consolidated approach: earthquake-induced landslide probabilities have been estimated in a strict statistical sense whereas floods have been estimated via a physics-based approach. The differences in the subsequent datasets and their inherent uncertainties means that a fully integrated probabilistic approach is not appropriate in this study, when we begin to consider the multi-hazard interactions.

3.1. Earthquake ground shaking

To provide ground shaking estimates for our predictive landslide model, we used a Ground Motion Model (GMM) to estimate ground shaking for selected plausible worst-case scenarios. We apply the GMM developed specifically for Türkiye and Iran by Kale et al. [42]. Scenario earthquakes were located at fault segments that were identified as seismic gaps based on historical events, static stress changes modelled using Coulomb stress transfer, and seismic gap analyses reported by Özacar et al. [43]. This led to the identification of six different fault ruptures (Table 2; Fig. 3): Malatya Fault, Kozan Fault, Adana Fault (Karataş–Türkoğlu segment), Antakya Fault, Dead Sea Fault and Bingöl Restraining Bend. The GMM by Kale et al. [42] returns peak ground acceleration (PGA) as a function of moment magnitude (Mw), Joyner–Boore distance (RJB), rupture type and Vs30. Earthquake magnitudes were estimated for each fault segment based on the length of the segment, using the empirical relationship proposed by Wesnousky [44] for strike-slip faults (Table 2). All scenario events were assumed to be vertically-dipping strike-slip ruptures. Vs30 values were adopted from [45], by extracting the Vs30 value in their dataset closest to each grid point. Ground motions were calculated on a 1 km × 1 km grid. The applied GMM was used to calculate expected ground motions for the 2023 M7.8 earthquake and compared to ground shaking as reported by the USGS ShakeMap system [33]. This visual comparison showed reasonable agreement, indicating that the chosen GMM is indeed appropriate for our study area.

Table 2
Earthquake scenarios considered in this study. Nr refers to the numbers in Fig. 3. Mw is the moment magnitude.

Nr	Fault	Rupture length (km)	Mw
1	Malatya Fault	174	7.5
2	Kozan Fault	137	7.4
3	Adana Fault (Karataş–Türkoğlu segment)	186	7.5
4	Antakya Fault	84	7.2
5	Dead Sea Fault	100	7.3
6	Bingöl Restraining Bend	44	7.0

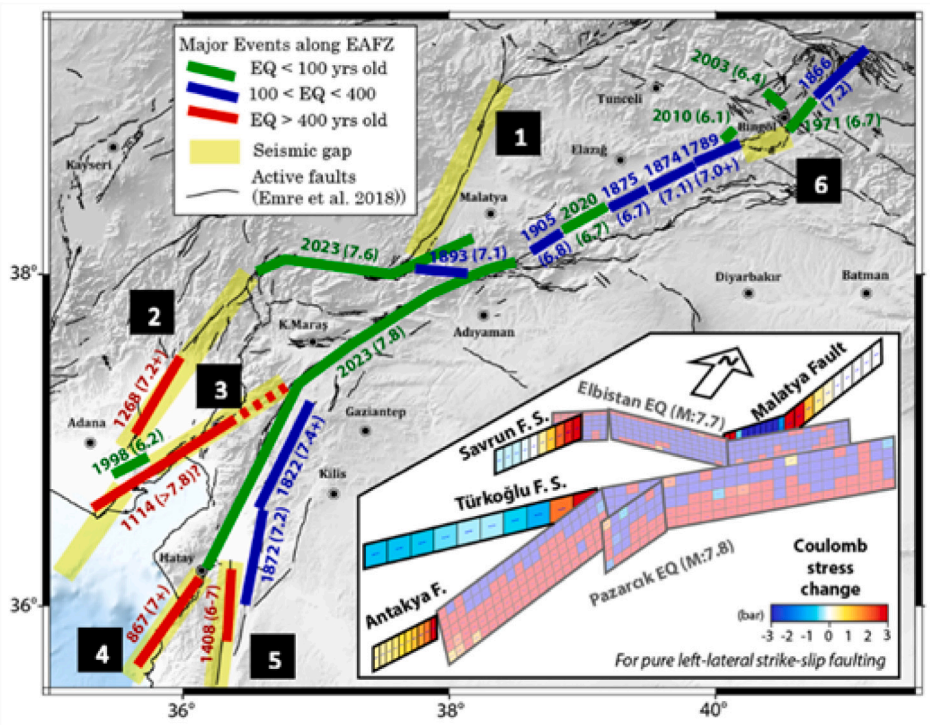

Fig. 3. Major fault segments and seismic gaps in the EAFZ area affected by the 2023 easrthquake sequence (adapted from Özacar et al. 2023). Numbers refer to the scenario numbers given in Table 2. Fault segments are from the Global Earthquake Model - Active Faults Database.

3.2. Landslides hazard

Landslides hazards have been calculated by Slope Unit (SUs; [46]) and extracted from our DTM with a total of 539,697 SUs derived. These SUs represent terrain units bounded by drainage and divide lines with similar geomorphological characteristics that, compared to pixel-based approaches, better reflect slope processes.

The inventory used for the GAM model comes from [12], which we expanded using Sentinel-2 satellite data available through the Google Earth Engine platform. GAM is a data-driven approach which allows for space–time modelling. GAMs enable modelling of non-linear relationships [47] between response and predictor variables — both triggering and predisposing factors [48]. Numerous examples can be found where this modelling framework constitutes the foundation for co-seismic landslide hazard assessment [49]. The strength behind this class of models resides in their ability to estimate highly nonlinear functional relations typical of advanced machine-learning tools, while offering a clear interpretation of the results typical of statistical techniques. In this project we adopted Integrated Nested Laplace Approximation (INLA) to fit the Bayesian framework of GAM, as it provides an efficient way to quantify model uncertainties [50]. For the response variable, our goal was to estimate the probability of co-seismic landslide occurrence, so we used a Bernoulli probability distribution, resulting in a binomial GAM. Each slope unit was therefore labelled as stable or unstable according to the absence or presence of landslides triggered by the 2023 earthquake.

We opted for five predictors to fit the binomial GAM: terrain morphology (slope angle and relief), lithological, seismic and deformation characteristics. Terrain-wise, we considered the mean slope steepness per SU as well as the relief, the latter being computed as the difference between the highest and the lowest elevation points within a SU. The rationale behind these two predictors is for the slope to carry the natural steepness effect on slope stability, whereas the relief is assumed to reflect the potential energy across to the landscape. Conversely, we chose the lithology to express the constitutive material of a given slope, a proxy for

geotechnical characteristics. It is important to stress that the GAM framework we designed features a training phase with respect to the observed co-seismic scenario in 2023, and a simulation phase where from the fitted model we solved for possible future configurations of the co-seismic landslide hazard. We mention this here because the terrain and lithological predictors we considered are landscape features that vary over long timescales.

Therefore, in both the training and simulation phases, we assumed them to stay the same. This is not the case for the two remaining predictors, which are inherently changing over space and time. Specifically, the InSAR-derived hillslope deformation, measured in mean annual velocity was calculated for pre-2023 and used as part of the training phase, whereas the post-2023 hillslope velocity is used for simulating future scenarios, thus reflecting the earthquake legacy effect onto the probabilistic hazard maps. We stress here that this information is an actual measurement, therefore, we would only have two hillslope velocity datasets, one for the training and one for the simulations. As for the other dynamic predictor, the earthquake intensity measured as PGA, multiple scenarios have been considered (see Section 3.1).

Modelling performance is assessed throughout the manuscript by means of Receiver Operating Characterising (ROC) curves and their Area Under the Curve (AUC), both being standard diagnostics of classification problems [51].

3.3. Flood hazard

Simulated both fluvial and flash flood using FastFlood, a rapid, web-based flood hazard simulation tool [10]. This physical numerical simulation model is coupled with an automated global parameterisation and scenario generation framework with processing time over a thousand times faster compared to conventional models, which is particularly beneficial for large-scale analyses [10]. The methodology is comprised of four key components: the core FastFlood computational method, the use of cascaded and adaptive grids for computational efficiency, a scenario pre-processing engine for defining boundary conditions, and a novel DTM filtering technique.

Input parameters were (see Table 1): topography, landcover, precipitation data, Sub-surface and Soil Properties, Rivers and Hydraulic Structures and Urban Infrastructure and Flood Protection. The model returns: (i) precipitation-driven and (ii) fluvial floods.

For precipitation-driven events, the model moves beyond traditional point-based Intensity-Duration-Frequency (IDF) curves and instead introduces Intensity-Duration-Frequency-Space (IDFS) curves. IDF curves describe the relationship between rainfall intensity, storm duration, and exceedance probability at a single point location, which become unreliable for large regions due to storm spatial variability. IDFS curves adds the spatial footprint of the storm to quantify how rainfall intensity changes in relation to the storm spatial extent, while maintaining the frequency-duration characteristics of extreme precipitation. These curves are derived from a global statistical analysis of GPM IMERG satellite precipitation data. This allows for the generation of spatially coherent design storms that accurately reflect the reduced average intensity, but higher localised peaks observed in real-world large-scale precipitation events. Although described as a curve, the IDFS is essentially a multidimensional surface which allows for realistic large-scale precipitation inputs to flood modelling — particularly for the size of our study region.

A "virtual precipitation" value, representing the higher local intensity, is used for infiltration calculations, while the spatially-averaged rainfall total is used for runoff routing, ensuring both soil saturation and total flood volume are modelled correctly. The climate change analysis is based on a full analysis of CMIP6 NASA downscaled climate projections. In order to quantify the range in outcomes present in the ensemble of climate models, 20 ensemble members were used, determining full extreme precipitation statistics from current period to 2100, and their changes.

For fluvial events, discharge boundary conditions are automatically placed and parameterised. The system uses HydroBasins river lines as a starting point, then employs a search algorithm on the high-resolution DTM to identify the true river channel thalweg for precise placement. Discharge values, for both hindcasts and forecasts, are derived from the GLObal Flood Awareness System (GLOFAS). These values are linked to the model's boundary locations by matching upstream drainage areas and are subsequently bias-corrected using a histogram-matching technique based on return period analysis to reconcile statistical differences between the global model and local conditions. A calibration and validation exercise was conducted for a study site within the transboundary region of Türkiye and Syria.

The primary objective of the calibration was to refine key model parameters to improve the match between simulated flood extents and observed inundation patterns, specifically: Manning's roughness coefficients for dominant land cover classes within the region, Soil infiltration parameters to better represent local soil responses to heavy rainfall and River channel conveyance parameters to better match the observed behaviour of local watercourses. The calibration process utilised observed flood extents derived from Sentinel-1 Synthetic Aperture Radar (SAR) imagery for a significant historical flood event. SAR imagery is particularly effective for this purpose as it can penetrate cloud cover, providing clear delineation of water bodies. The observed flood footprint was compared against the model's simulated maximum inundation extent.

Model performance was quantitatively assessed using spatial comparison metrics, such as the Critical Success Index (CSI), which measures the spatial overlap between simulated and observed flooding while penalising both over- and under-prediction. Parameters were systematically adjusted to maximise the CSI score.

Following the calibration phase, the model was validated against a separate, independent flood event that was not used during the parameter tuning process (the March 2023 event in the Adıyaman's Tut district). This crucial step ensures that the model was not simply "overfitted" to a single event and that the calibrated parameter set has genuine predictive power for future events under different conditions. The validation results confirmed that the calibrated model could reproduce the extent and pattern of the independent flood event with a high degree of fidelity.

3.4. Multi-hazard approach

To produce the multi-hazard susceptibility map, we combined the individual hazard footprints using TOMRAP, a semi-open-source framework developed by the British Geological Survey. TOMRAP provides a structured workflow for integrating heterogeneous hazard datasets by resolving differences in spatial resolution, grid alignment, coordinate reference systems and value ranges prior to combination. The first output is a multi-hazard susceptibility map, while the second integrates exposure data, and building vulnerability parameters link to the Global Earthquake Model building taxonomy [52]. The original code was adapted to fit the data and workflow of this study, and an overview is given below.

Within the TOMRAP framework, the initial hazard map inputs are aligned to a common spatial framework. Ensuring that the flood and co-seismic landslide raster layers are the same coordinate reference system, spatial extent, pixel size (defined by the coarsest resolution dataset) and grid alignment, the framework adjusts as necessary. Meaning, where difference occurs, rasters were resampled to the smallest consistent pixel size to allow direct, pixel-by-pixel comparison. Where either Invalid or NoData values are embedded within the raster, each input is standardised to prevent artefacts during combination. Additionally, common Sentinel values (e.g. −9999) were converted to null values so that they did not influence subsequent aggregation or normalisation steps within the framework.

The co-seismic landslide output consists of a raster of landslide occurrence probabilities at the slope-unit scale, which were directly normalised to a range of 0–1. The flood hazard layer comprised two components: maximum flood depth and inundation extent. Flood depth values were normalised to a 0–1 range, while inundation extent was represented as a binary layer where 1-in-50-year flooded pixels were assigned a value of 1 and non-flooded pixels a value of 0. The final flood hazard index was calculated as the maximum value of these two layers, ensuring that either deep flooding or widespread inundation resulted in elevated flood hazard representation. Following normalisation, both flood and landslide layers were transformed into ordinal hazard classes (0–5) using their quantile distribution since they represent different physical quantities (e.g. flood depth versus landslide susceptibility). Each raster was transformed to a common ordinal hazard scale prior to combination. Specifically, non-zero raster values were reclassified to an index ranging from 1 to 5 using a quantile-based classification, while zero and no-data values were assigned to class 0. For example, the thresholds between the five non-zero classes were defined using the 20th, 40th, 60th, and 80th percentiles of the positive values within each raster. Accordingly, class 1 corresponds to the lowest 20% of non-zero values, class 2 to the next 20%, and so on, with class 5 representing the highest 20% of non-zero values.

This approach does not imply that the resulting classes correspond to fixed physical process thresholds. Rather, it provides a data-driven and reproducible way to express relative hazard intensity within each input layer, thereby allowing heterogeneous datasets with different units and value ranges to be combined in a consistent multi-hazard framework. The resulting indexed layers should therefore be interpreted as ordinal rankings of relative hazard, not as absolute physical magnitudes.

The six individual co-seismic landslide susceptibility maps, with each representing a distinct fault-rupture scenario, were first combined into a single hazard layer. A worst-case approach was adopted, whereby the maximum susceptibility value was selected for each SU across all six scenarios. The result is a single co-seismic landslide raster which captures the highest potential hazards at each location, independent of which rupture scenario occurs (50 m). The flood hazard however, is represented by a single flood hazard raster corresponding to the 1-in-50-year return period (30 m). To ensure full consistency between the two hazard types, the flood layer was processed using the same spatial harmonisation and normalisation steps applied to the landslide rasters.

After reducing the inputs to one landslide hazard raster (worst-case across scenarios) and one flood hazard raster, TOMRAP combined them into a single multi-hazard index using a weighted overlay approach according to:

MH Susceptibility = wLH + wFH

Where the weighted landslide hazard (wLH), produced from the combined co-seismic scenarios, is combined with the weighted flood hazard (wFH), to obtain the relative multi-hazard susceptibility of each pixel (50 m).

In this formulation, the indexed flood and co-seismic landslide hazards contribute proportionally to the final score through assigned weights representing the hazards combination. In this study, equal weights were applied to both hazard layers. In the original TOMRAP methodology, weighting factors were determined by the availability of either hazard frequency magnitude distributions or else by damage/loss data. From here, it is possible to calibrate the hazards relative to each other. In this study however, the choice to use equal weightings reflects the fact that the six co-seismic landslide scenarios were first consolidated into a single worst-case raster, resulting in one representative landslide input and one flood input. In the absence of a robust empirical basis for prioritising one hazard over the other, equal weighting was adopted as a transparent baseline assumption rather than a calibrated representation of relative hazard importance. The use of equal weights also avoids imposing subjective prioritisation between the different hazards. The two hazard datasets were generated using fundamentally different modelling paradigms (deterministic earthquake-triggered landslides vs. probabilistic 1-in-50-year return period flood scenarios) and are not temporally synchronised, no attempt is made to estimate joint probabilities or causal interactions, as uncertainties generated in the creation of the original hazard datasets could be compounded and amplified in a probabilistic approach. The objective of this study is to ultimately identify the spatial co-occurrence rather than joint probability, therefore the resulting output should be interpreted as an index-based representation of relative multi-hazard conditions, rather than a probabilistic or impact-calibrated risk model.

TOMRAP is programmed to produce a multi-hazard risk map by integrating exposure (number of buildings) and vulnerability (building characteristic) data with the hazard index. The original framework was designed to be aligned with the GEM building taxonomy, which standardises building classification based on properties such as building usage, construction materials, number of storeys and construction period, thereby enabling the application of vulnerability functions. For the purpose of this study, the framework was adapted to allow the use of gridded population density data, specifically the WorldPop dataset for 2020, as a proxy for exposure. This modification enables the estimation of population exposure to multi-hazard conditions; however, it does not explicitly account for vulnerability, as no population-specific vulnerability functions are applied.

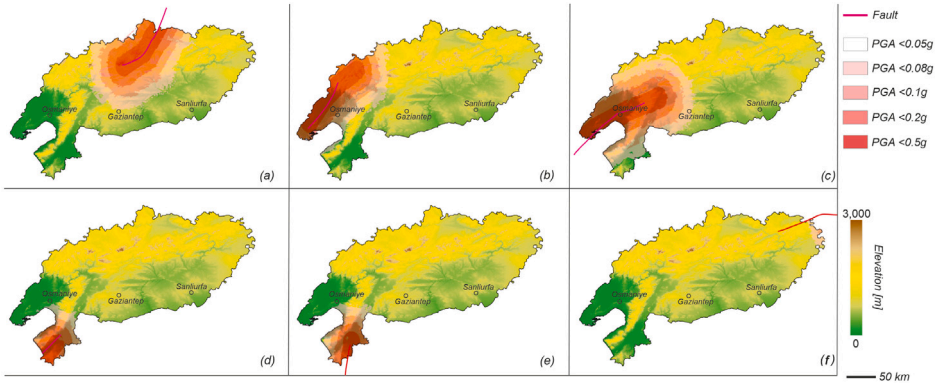

Fig. 4. Maps for the ground shaking distribution for six scenarios: (a) Malatya; (b) Kozan Fault; (c) Adana Fault; (d) Antakya Fault; (e) Dead Sea Fault; (f) Bingöl restraining bend. Fault segments are from the Global Earthquake Model - Active Faults Database. Background map is the hillshade topography from the NASA Shuttle Radar Topography Mission (SRTM).

4. Results

4.1. Earthquake ground shaking

The spatial distributions of PGA for the six ground-shaking scenarios are shown in Fig. 4. Together, these ground shaking estimates illustrate how fault-specific rupture characteristics shape the expected spatial distribution of shaking across southeastern Türkiye.

Each deterministic scenario (Fig. 4a–f) reflects the characteristic rupture geometry, magnitude, and location of a specific fault segment within the EAFZ system. As a result, the high-intensity shaking is concentrated along the corresponding fault trace and decays rapidly with increasing distance from the rupture. The ground motion field is not completely symmetric around the rupture due to spatial variation in VS30. The largest PGA values occur around the modelled fault rupture, where peak accelerations locally exceed 0.4–0.6 g, depending on rupture length and thus magnitude. The spatial footprint of strong ground motion expands noticeably for scenarios involving longer segments. Furthermore, as expected, scenarios located centrally within our study area will have a larger effect here. For example, ruptures along the Malatya (Fig. 4a) and Antakya (Fig. 4d) faults produce widespread shaking across densely populated areas in the northern and southern portions of the study region, whereas scenarios located further east or on shorter segments lead to more spatially confined areas of elevated PGA within our study area. Across all scenarios, ground motions extend far beyond the immediate fault rupture, with moderate PGA values (0.1–0.2 g) covering large portions of the study area despite the attenuation. These broad, lower-intensity PGA fields are particularly relevant for the landslide simulations, as even moderate shaking levels can contribute to widespread hillslope destabilisation in susceptible terrain.

4.2. Landslides

The probabilistic maps of co-seismic landslide occurrence for the six shaking scenarios are shown in Fig. 5 and are expressed as posterior mean probabilities at SU scale.

Among the deterministic segment ruptures, the Malatya scenario concentrates elevated probabilities in the central sector of the study area (Fig. 5a), whereas Kozan shifts the highest values north-westwards, reflecting differences in shaking directionality and attenuation (Fig. 5b). The Adana rupture emphasises a central–western swath of high susceptibility (Fig. 5c), while Antakya (Fig. 5d), Dead Sea (Fig. 5e), and Bingöl (Fig. 5f) produce patterns that are distinct. The latter provides the most representative mid-probability forecast, bridging the gap between fault-specific rupture hypotheses and the statistically rare extremes. As such, it offers a practical and policy-relevant hazard layer, particularly in areas where it spatially coincides with post-seismic acceleration detected in InSAR. The partial overlap of high-landslides hazard zones in the Antakya, Dead Sea, and Bingöl rupture scenarios indicates the presence of localised hotspots where moderate-to-strong shaking repeatedly interacts with steep slopes, susceptible lithologies, and pre-existing deformation. Despite its low likelihood, this representation remains physically meaningful as a design-level stress test for emergency preparedness and infrastructure resilience.

Although all scenarios share identical static terrain properties and lithology, the spatial organisation and intensity of high-probability clusters vary substantially depending on the imposed ground-shaking field. This behaviour demonstrates that the GAM-INLA framework responds coherently to the scenario-specific PGA patterns, while retaining sensitivity to local topographic and geological controls.

The estimated effects of the predictors included in the binomial GAM are presented in Fig. 6, together with their associated posterior uncertainties. The first panel represents the global intercept (Fig. 6a) quantifies the baseline log-odds and corresponding probability of observing a co-seismic landslide in any given slope unit before accounting for the influence of any predictors. In other

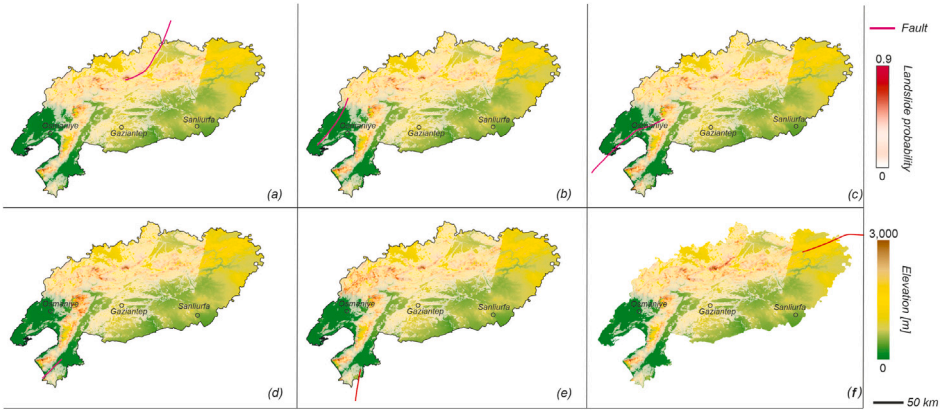

Fig. 5. Deterministic hazard maps fo coseismic landslide occurences for six scenarios: (a) Malatya; (b) Kozan Fault; (c) Adana Fault; (d) Antakya Fault; (e) Dead Sea Fault; (f) Bingöl restraining bend. The corresponding seismogenic fault for each scenario is mapped respectively. Fault segments are from the Global Earthquake Model - Active Faults Database. Background map is the hillshade topography from the NASA Shuttle Radar Topography Mission (SRTM).

words, the intercept can be interpreted as the empirical probability of failure expected for a "typical" slope unit if no information were available about its terrain characteristics, lithology, PGA level, or pre-earthquake deformation. This value reflects the overall prevalence of landslides in the 2023 inventory and provides the reference point from which all other predictor effects act additively. A relatively low global intercept is consistent with the fact that only a small fraction of slope units in the study region experienced co-seismic failure, while substantial deviations from this baseline arise once slope steepness, relief, lithology, and shaking intensity are incorporated through the predictor terms. All predictors exhibit statistically significant contributions to the probability of co-seismic landslide occurrence, and the model behaviour aligns well with expected geomorphological controls. The effect of PGA is positive, as expected, indicating that stronger ground motion increases the likelihood of slope failure. While the relationship is linear in the model, the posterior credible intervals remain narrow, demonstrating that the 2023 landslides provide a robust empirical basis for constraining the shaking–landslide relationship. This consistency across scenarios is important because PGA is the only predictor that changes across the forward simulations (Fig. 6b). Relief, representing the local elevation range within each slope unit, exerts a positive linear effect on landslide occurrence (Fig. 6c). Larger relief values correspond to higher potential energy contrasts and deeper gravitational energy wells, and the model captures this by assigning increasingly positive coefficients as relief increases. Slope steepness emerges as the most influential variable among the predictors (Fig. 6d).

The spline function shows a strong, consistently positive effect, with steeper slopes associated with markedly higher landslide probabilities. This behaviour is reflected in narrow 95% percentile intervals and high regression magnitudes. The same can be seen for the slope, not only significant but also associated with the highest regression coefficients, diagnostic of a large control on the co-seismic landslide occurrence probabilities.

Together, slope and relief highlight the importance of terrain morphology in controlling shaking-induced failure. The predictor describing pre-2023 event hillslope deformation (mean annual velocity) displays a more complex, nonlinear effect (Fig. 6e). Low to moderate deformation rates are generally associated with lower failure probability, whereas higher absolute velocities, whether upslope or downslope, lead to positive contributions. This pattern supports the hypothesis that slopes already experiencing measurable, long-term deformation are more susceptible to co-seismic acceleration and failure. Uncertainties widen at higher velocity magnitudes due to fewer observations, but the underlying trend remains evident. Ultimately, each of the four lithological classes also appeared to be statistically significant (Fig. 6f), with metamorphic, ophiolithic and sedimentary classes being consistently positive, as opposed to plutonic and volcanic classes acting to locally reduce the co-seismic landslide occurrence probabilities. These differences point to the key mechanistic role of substrate strength and weathering behaviour in modulating co-seismic susceptibility.

For the validation, we artificially split the whole study area into ten random subsets, each mutually exclusive and representative of 10% of the whole sample. In turn, merging the ten subsets together again would return the whole study area once more, demonstrating that our ten-fold cross-validation strategy efficiently tests our model against all the possible variability that the landscape under consideration presents. This procedure then translated into training our binomial GAM over 9 subsets and validating the prediction over the remaining one, iterating this for each of the 10 random subsets. Overall, the estimated effect plots confirm that the GAM successfully captures both the primary physical controls on co-seismic landsliding and the more subtle contributions from pre-existing slope conditions and lithology (Fig. 7). The model's strong performance in the cross-validation analysis (AUC = 0.85–0.89) further supports its suitability for simulating future co-seismic landslide scenarios under varying combinations of hillslope deformation and PGA. The spatial patterns emerging from these simulations are discussed in the context of compounding hazards in Section 4.4.

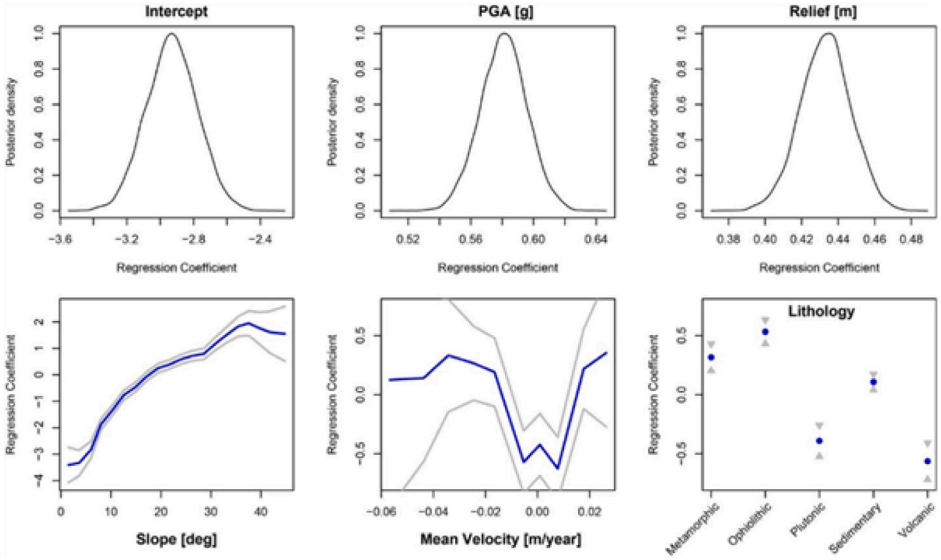

Fig. 6. The effects of estimated predictors on landslides hazard. Besides the global intercept (a), the PGA (b) and relief (c) are used linearly, whereas slope (d) and mean annual velocity (e) are used as splines. Ultimately, lithology is passed to the model as a categorical term (f). Elements colour coded in blue represent posterior mean values whereas the areas between grey symbols represents the 95% credible intervals.

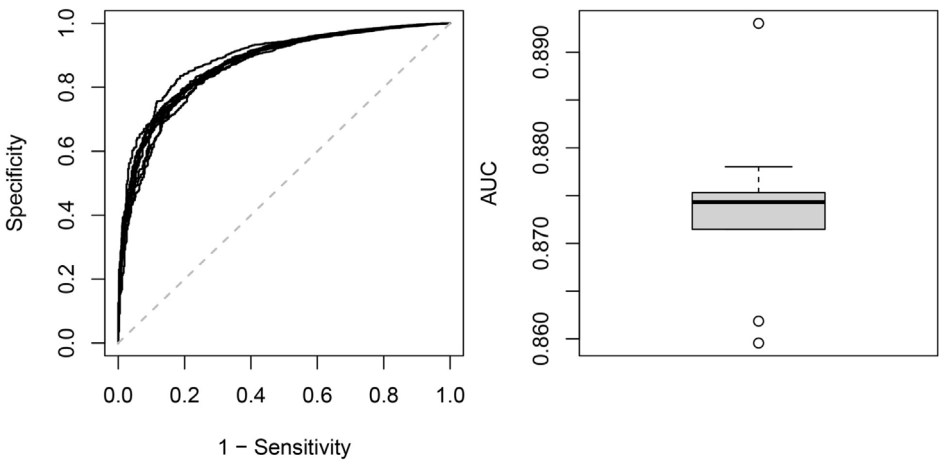

Fig. 7. Receiver Operating Curves (ROC) curves (left) and their integral values (right) estimated for each of the 10 cross-validation folds.

4.3. Floods

Flood hazard results for the study region are summarised in Fig. 8, where we present only the 50-year return period simulations. The flood maps depict both the spatial extent of inundation and the associated water depths (in metres), enabling the identification of areas at risk from both shallow, widespread flooding and deeper, more hazardous flow conditions. Overall, the 50-year flood scenario shows substantial inundation along the major river valleys (Ceyham River, Asi River and Euphrates) and low-lying basins. which will influence the combined multi-hazard footprint discussed later.

Specifically, meandering floodplain shows alternating bands of high and moderate hazard corresponding to active meander belts, natural levees, and low-lying swales. Consistently, high-hazards zones correspond to the widening of downstream sections where valley gradients decrease and floodwaters spread across broad alluvial plains, tributary confluences and mountain-front alluvial fans, where steep upstream catchments deliver rapid inflows that accumulate on lower-gradient surfaces.

The deepest floodwaters (up to 28 m, which may coincide with reservoirs, dams or existing water bodies) occur in confined floodplains and downstream reaches where topography funnels flow, while broader alluvial plains tend to experience shallower but spatially extensive flooding. Urbanised areas located near river channels, particularly those with limited drainage capacity, also show pockets of elevated flood depth, reflecting both hydrodynamic amplification and local infrastructure constraints. The FastFlood

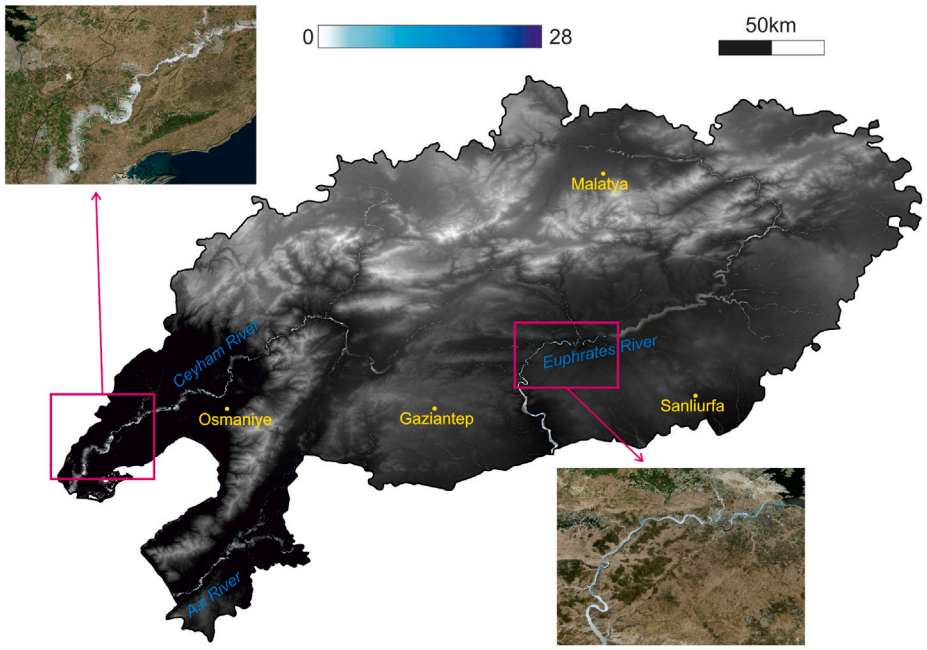

Fig. 8. Final calibrated flood hazard maps for the study site in the Türkiye-Syria border region, presenting simulated inundation for a 50-year return period with zoom-in for the Ceyham River (top-left corner) and Euphrates River (bottom-right corner). Background map is the hillshade topography from the NASA Shuttle Radar Topography Mission (SRTM).

modelling framework used in this study is optimised for representing fluvial (riverine) flooding, which is driven by upstream discharge and channel hydraulics. As such, the maps should be interpreted primarily as indicators of river-related inundation under extreme precipitation and flow conditions, rather than detailed representations of flash floods. Although the model includes a rainfall-driven component, locally triggered flash floods, typically governed by short-lived, high-intensity storms in steep terrain, are not fully resolved at this regional scale. Consequently, the flood hazard maps are best suited for identifying risks related to longer-duration fluvial events, which are most relevant for evaluating impacts on riverine infrastructure, embankments and fluvial dams. By contrast, flash floods play a more dominant role in debris-flow initiation and other rapid geomorphic responses, but these cascading processes fall outside the scope of the current analysis.

4.4. Compounding, multi-hazard map

By combining the indexed flood and co-seismic landslide hazard rasters using the weighted linear combination, the TOMRAP framework produced a multi-hazard susceptibility map that reflects the relative spatial coincidence of the two hazards. The co-seismic landslide input represents the worst-case envelope across the six rupture scenarios, while the flood input corresponds to the 50-year return-period flood hazard raster. Because tThe final integration involved one flood layer and one landslide layer, equal weighting was adopted as a transparent baseline assumption. The hazard values were first transformed to a common ordinal scale ranging from 0 (no hazard) to 5 (highest relative hazard) using quantile-based classification, allowing datasets with different units and value ranges to be combined consistently.

The resulting map (Fig. 9) highlights the spatial variation of relative multi-hazard susceptibility, with higher scores expressed by darker red colours indicating areas where flood and co-seismic landslide hazards spatially coincide. This output should be interpreted as an index-based representation of relative multi-hazard conditions, rather than a calibrated probabilistic risk model. Multi-hazard risk can then be explored separately by incorporating vulnerability and overlaying exposure datasets such as buildings or population onto the final hazard index. The method that we have used is flexible enough to allow for independent weighting of both separate hazards and a number of vulnerability factors, dependant on available data, producing a data driven semi-quantitative multi-hazard risk assessment. Testing of different weighting combinations and investigation of subsequent residual outputs can be linked to historic loss data to give an estimate of potential future loss.

The susceptibility map highlights locations where the hazards spatially coincide, which are typically:

- Valley margins where steep slopes transition into floodplains
- Mountain fronts adjacent to urban and sub-urban drainage networks
- Areas where earthquake-induced slope instability may interact with hydrological processes within the 50-year timeframe

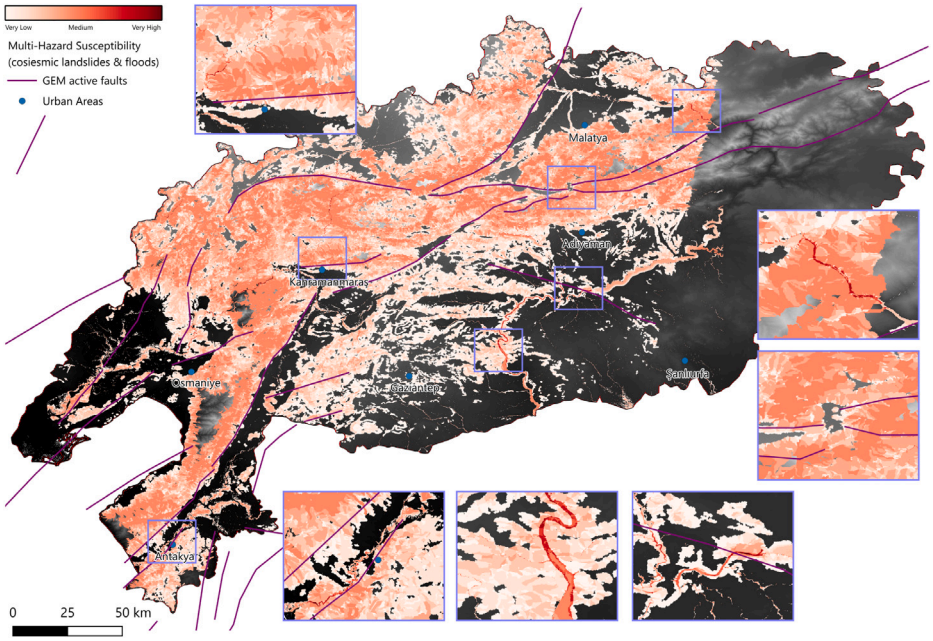

Fig. 9. Multi-hazard map for the study region, equally considering flood and co-seismic landslide hazards. Data presented at 50 m spatial resolution for the study area.

Table 3
Number of buildings and people exposed to different hazard levels.

Hazard class	No. Buildings	No. People
Class 1 (very low)	430,248	3,723,316
Class 2 (low)	215,020	1,066,730
Class 3 (medium)	57,130	251,888
Class 4 (high)	295	2,202
Class 5 (very high)	118	852
Null value	1,352,026	4,669,477

Although the spatial overlap between both high landslide susceptibility and high flood hazard is relative, the areas identified highlight areas where communities and infrastructure may be exposed to multiple hazard types within the same planning and life-cycle period. For example, linear features (e.g. roads and rail) alongside river valleys show an elevated multi-hazard susceptibility, linked to steep valley walls, anthropogenic geomorphological change and high flood depths.

The map does not imply simultaneous occurrence or dynamic hazard interactions due to the nature of the input data, but aids as a practical tool for the identification of areas where multiple hazards could impact the same assets over a given time-frame.

With the susceptibility map, we conducted several integrations of exposure data to begin to conceptualise the elements that may be at risk. It is important to mention that there was no vulnerability data explicitly used within this methodology, due to data availability and large spatial extent. Using a simple overlay of the WorldPop 2020 population data and the GEM building footprints, we can quantify the hazard susceptibility in relation to the number of people and assets (Table 3).

Table 3 shows that the vast majority of buildings (~645,000) and people (~4.8 million) are located in areas classified as very low to low multi-hazard susceptibility (Classes 1–2). Exposure decreases sharply with increasing hazard level, with only 57,130 buildings and ~252,000 people falling within the medium class. High and very high hazard zones contain a very small proportion of assets, fewer than 420 buildings and 3000 people combined, yet these areas represent critical hotspots where landslide- and flood-prone terrain coincide. The large number of features labelled as "Null Value" reflects areas excluded due to missing data or raster alignment limits and should therefore not be interpreted as hazard-free. Alongside the overlay, the TOMRAP framework was adjusted to integrate a population density raster — opposed to the traditional building taxonomy, allowing the exposure mapped in relation to the multi-hazards (Fig. 10). This coincides with the population overlay results, showing urban and sub-urban areas that have a high density of people coinciding with a high multi-hazard susceptibility.

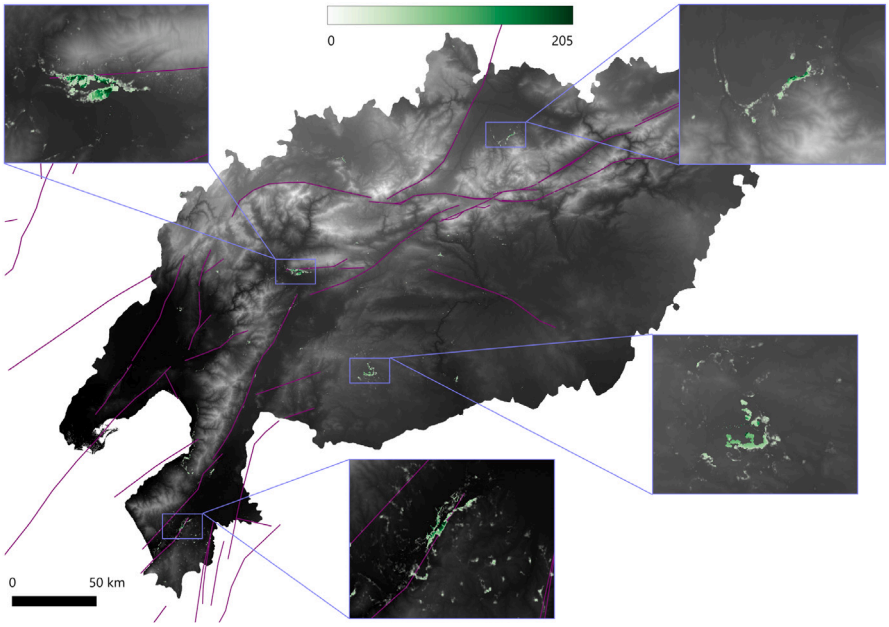

Fig. 10. Map highlighting population density results via adapted TOMRAP framework, in reference to the co-seismic landslide and flood multi-hazard susceptibility. Number of people per square kilometer.

5. Discussion and conclusions

The 2023 Kahramanmaraş Earthquake Sequence exemplifies the extent to which seismic, geomorphic, and hydrometeorological processes interact to generate cascading and compounding risks across southeastern Türkiye. The integrated modelling framework developed in this study, combining scenario-based ground shaking, co-seismic landslide susceptibility and 50-year fluvial flood hazards, provides one of the first regional-scale assessment of future multi-hazard conditions in this area and understanding of where such interactions matters the most, offering a basis for prioritising future detailed investigations. By harmonising heterogeneous datasets and employing the TOMRAP workflow to combine distinct hazard layers, the analysis reveals persistent spatial patterns of overlapping hazards and identifies areas where communities and infrastructure may remain exposed to elevated susceptibility over the coming decades.

Each model component includes a validation strategy designed to quantify predictive performance. Ground-shaking scenarios were evaluated qualitatively against USGS ShakeMap products for the 2023 KES, showing reasonable spatial agreement. The landslide model demonstrated robust predictive capability (AUC = 0.85–0.89) across ten spatially independent cross-validation folds, confirming its skill in capturing the key geomorphic and seismic controls. Flood modelling underwent calibration using SAR-derived inundation extents for a historical event, followed by validation against an independent case; both exercises produced high spatial correspondence as measured by the Critical Success Index. While these validations support the reliability of individual components, uncertainties propagate through the multi-hazard combination, particularly where hazard layers with differing resolutions converge.

Our results show that multi-hazard hotspots emerge where strong ground motion repeatedly coincides with steep topography, susceptible lithologies, and fluvial corridors. These domains include the northern and central portions of the affected region, where co-seismic landslide susceptibility is consistently high across rupture scenarios, as well as major valley systems such as the Ceyhan, Orontes and Euphrates rivers, where the 50-year fluvial flood model predicts widespread inundation. When combined, these patterns result in concentrated multi-hazard susceptibility along mountain fronts, valley margins, and transitional slope–river environments. Within these zones, approximately 702,000 buildings and 5.0M people fall within the mapped hazard classes but only 118 buildings and 850 residents located in the highest hazard category. While these numbers are not directly predictive of losses, they underline the scale of long-term exposure across an already vulnerable landscape. The spatial co-location of landslides and floods reflects the interplay between geomorphology and hydrodynamics under both current and future conditions. Landslide-prone slopes commonly transition into sediment-rich floodplains where channel capacity is limited and floodwaters accumulate. Conversely, valleys with high fluvial hazard often mark areas where strong ground shaking can destabilise adjacent slopes. These relationships are consistent with global observations of compounding post-earthquake hazards, where weakened hillslopes, altered drainage networks, for example damming the river course, and contribute to prolonged periods of risk.

We highlight some limitations of our current work:

Importantly, the combined multi-hazard map reflects potential co-occurrence rather than direct triggering. While earthquakes may initiate landslide dams or sediment pulses that influence downstream flooding, these dynamic interactions require process-specific modelling. The present approach focuses on the spatial convergence of independent hazards, an appropriate basis for

long-term risk planning, infrastructure design and prioritisation of monitoring but not short-term crisis forecasting. The modelling framework does not simulate the dynamic evolution of slopes or hydrological systems over time. Processes like progressive weathering, rainfall-induced pore-pressure changes, sediment redistribution or delayed failure of seismically affected slopes are not explicitly represented in the co-seismic landslide approach. Additionally, the flood model does not incorporate sediment pulses, channel blockages or altered drainage pathways that may arise from the co-seismic landslides. This could be incorporated via long-term observational datasets in the future.

The multi-hazard analysis rests on a statistical method for landslides and physical model for floods with assumptions inherent to each modelling component. For seismic shaking, GMM represents ruptures using homogeneous mechanics and simplified attenuation and the six rupture scenarios collectively approximate a set of physically plausible, but not exhaustive, future events. The choice to adopt a worst-case envelope across scenarios is reasonable for future long-term risk assessment but may overestimate hazard intensity in some locations.

We acknowledge that the landslide susceptibility maps are derived from deterministic earthquake scenarios, whereas the flood hazard corresponds to a probabilistic 1-in-50-year return period. These layers therefore occupy different positions in probability space. Because our objective is to identify spatial co-occurrence rather than joint probability, we combine them using a normalised index rather than a probabilistic formulation. A full joint probability model would require a multivariate hazard framework (e.g., [39,40]), which is beyond the scope of this study but represents an important direction for future work.

The co-seismic landslide model (GAM with INLA estimation) assumes static lithology and terrain for both training and simulation phases. While reasonable for a 50-year horizon, this approach does not account for long-term hillslope evolution, regolith development or earthquake-induced slope recovery. The deformation predictor is limited to two epochs (pre-2023 and post-2023) restricting the temporal characterisation of slope acceleration or deceleration. Similarly, the reliance on slope units provides geomorphologically meaningful boundaries but constrains the spatial resolution of the susceptibility output.

For flood hazard modelling, FastFlood primarily captures large-scale fluvial inundation and precipitation-driven events using CMIP6-derived climate scenarios. It does not simulate sediment transport, bank erosion, debris-rich flows, or landslide dam outburst floods. These processes might be important in post-earthquake environments but require dedicated sediment–hydrology coupling beyond the scope of this analysis. Consequently, the flood layers presented here reflect hydrodynamic inundation patterns rather than the full spectrum of mass-flow hazards.

Finally, TOMRAP integrates hazards at a common resolution but necessarily involves downscaling and upscaling of input datasets ranging from 5 m DTM-derived slope units to 1 km demographic projections. While these transformations enable consistent analysis, they also introduce smoothing effects that should be considered when interpreting local-scale results.

Despite these limitations, which can be addressed in future work, our study provides a valuable basis for long-term disaster risk reduction in southeastern Türkiye where hazard drivers coexist and interact in terms of:

- Regional planning, by identifying areas where reconstruction should account for overlapping hazards rather than single-hazard design criteria.
- Infrastructure resilience, particularly along transport corridors, where slopes and river crossings create recurrent points of vulnerability.
- Scenario-based emergency preparedness, by offering a consistent method to evaluate how future earthquakes and extreme precipitation events may interact spatially.

The dataset is freely available while the methodology workflow is modular and transferable, allowing adaptation to other tectonically active regions facing similar combinations of seismic and hydrometeorological hazards.

CRediT authorship contribution statement

E. Mills: Writing – original draft, Formal analysis, Conceptualization. **R. Chahel:** Validation, Software, Data curation. **H. Hourston:** Resources, Investigation, Data curation. **A. Winson:** Software, Methodology, Conceptualization. **M.B. Sørensen:** Writing – original draft, Methodology, Investigation, Funding acquisition, Data curation, Conceptualization. **L. Lombardo:** Writing – original draft, Project administration, Methodology, Funding acquisition, Formal analysis, Conceptualization. **E. Hussain:** Writing – review & editing, Formal analysis, Conceptualization. **B. Van den Bout:** Writing – original draft, Software, Methodology, Formal analysis, Data curation. **H. Tanyas:** Writing – original draft, Validation, Methodology, Data curation, Conceptualization. **A. Novellino:** Writing – original draft, Supervision, Project administration, Methodology, Funding acquisition, Formal analysis, Data curation, Conceptualization.

Declaration of competing interest

The authors declare the following financial interests/personal relationships which may be considered as potential competing interests: Alessandro Novellino reports financial support was provided by European Space Agency [40000144311/24/I-KE]. All other authors declare that they have no known competing financial interests or personal relationships that could have appeared to influence the work reported in this paper.

Data availability

Data will be made available on request.

References

[1] X. Fan, G. Scaringi, O. Korup, A.J. West, C.J. Van Westen, H. Tanyas, N. Hovius, T.C. Hales, R.W. Jibson, K.E. Allstadt, L. Zhang, Earthquake-induced chains of geologic hazards: Patterns, mechanisms, and impacts, Rev. Geophys. 57 (2) (2019) 421–503, http://dx.doi.org/10.1029/2018RG000626.

[2] M.E. Kincey, N.J. Rosser, T.R. Robinson, A.L. Densmore, R. Shrestha, D.S. Pujara, K.J. Oven, J.G. Williams, Z.M. Swirad, Evolution of coseismic and post-seismic landsliding after the 2015 Mw 7.8 Gorkha earthquake, Nepal, J. Geophys. Res.: Earth Surf. 126 (3) (2021) e2020JF005803, http://dx.doi.org/10.1029/2020JF005803.

[3] O. Korup, Landslide-induced river channel avulsions in mountain catchments of southwest New Zealand, Geomorphology 63 (1–2) (2004) 57–80, http://dx.doi.org/10.1016/j.geomorph.2004.03.005.

[4] R.N. Parker, G.T. Hancox, D.N. Petley, C.I. Massey, A.L. Densmore, N.J. Rosser, Spatial distributions of earthquake-induced landslides and hillslope preconditioning in the northwest South Island, New Zealand, Earth Surf. Dyn. 3 (4) (2015) 501–525, http://dx.doi.org/10.5194/esurf-3-501-2015.

[5] G. Karakas, S. Kocaman, C. Gokceoglu, Multi-hazard susceptibility assessment with hybrid machine learning methods for tut region (Adiyaman, Turkiye), in: The International Archives of the Photogrammetry, Remote Sensing and Spatial Information Sciences, Vol. 48, 2023, pp. 529–536, http://dx.doi.org/10.5194/isprs-archives-XLVIII-M-1-2023-529-2023.

[6] E. Bozkurt, S.K. Mittwede, Introduction to the geology of Turkey—A synthesis, Int. Geol. Rev. 43 (7) (2001) 578–594, http://dx.doi.org/10.1080/00206810109465034.

[7] T. Görüm, S. Fidan, Spatiotemporal variations of fatal landslides in Turkey, Landslides 18 (5) (2021) 1691–1705, http://dx.doi.org/10.1007/s10346-020-01580-7.

[8] I. Haltas, E. Yildirim, F. Oztas, I. Demir, A comprehensive flood event specification and inventory: 1930–2020 Turkey case study, Int. J. Disaster Risk Reduct. 56 (2021) 102086, http://dx.doi.org/10.1016/j.ijdrr.2021.102086.

[9] T. Görüm, D. Bozkurt, O. Korup, E. İstanbulluoğlu, Ö.L. Şen, A. Yılmaz, F. Karabacak, L. Lombardo, B. Guan, H. Tanyas, The 2023 Türkiye-Syria earthquake disaster was exacerbated by an atmospheric river, Commun. Earth Environ. 6 (1) (2025) 151, http://dx.doi.org/10.1038/s43247-025-02111-9.

[10] B. Van den Bout, V.G. Jetten, C.J. van Westen, L. Lombardo, A breakthrough in fast flood simulation, Environ. Model. Softw. 168 (2023) 105787, http://dx.doi.org/10.1016/j.envsoft.2023.105787.

[11] A. Winson, K. Smith, K. Leeming, D. Valters, R. Ciurean, Forewarned is forearmed: Understanding multihazard risk assessment methods for disaster risk reduction and for increasing disaster preparedness, 2023, Unpublished. Available at: https://nora.nerc.ac.uk/id/eprint/536668/. Lecture presented at the 59th CCOP Annual Session, Phang Nga, Thailand.

[12] T. Görüm, H. Tanyas, F. Karabacak, A. Yılmaz, S. Girgin, K.E. Allstadt, M.L. Süzen, P. Burgi, Preliminary documentation of coseismic ground failure triggered by the February 6, 2023 Türkiye earthquake sequence, Eng. Geol. 327 (2023) 107315, http://dx.doi.org/10.1016/j.enggeo.2023.107315.

[13] X.X. Zhu, Q. Li, Y. Shi, Y. Wang, A.J. Stewart, J. Prexl, F. Zhang, GlobalBuildingMap—Unveiling the mystery of global buildings, Sci. Data 13 (2026) 71.

[14] T.Y. Duman, Ö. Emre, The East Anatolian Fault: Geometry, segmentation and jog characteristics, in: Special Publications, Vol. 372, Geological Society of London, 2013, pp. 495–529, http://dx.doi.org/10.1144/SP372.14.

[15] E. Herece, Doğu Anadolu Fayı (DAF) Atlası, Special Publications, General Directorate of Mineral Research and Exploration (MTA), Ankara, 2008, Serial Number unspecified.

[16] A.M.C. Şengör, M. Yazıcı, The aetiology of the neotectonic evolution of Turkey, Mediterr. Geosci. Rev. 2 (2020) 327–339, http://dx.doi.org/10.1007/s42990-020-00039-0.

[17] E. Hussain, T.J. Wright, R.J. Walters, D.P. Bekaert, R. Lloyd, A. Hooper, Constant strain accumulation rate between major earthquakes on the North Anatolian Fault, Nat. Commun. 9 (1) (2018) 1392, http://dx.doi.org/10.1038/s41467-018-03739-2.

[18] A.I. Kurt, A.D. Özbakir, A. Cingöz, S. Ergintav, U. Doğan, S. Özarpaci, Contemporary velocity field for Turkey inferred from combination of a dense network of long term GNSS observations, Turk. J. Earth Sci. 32 (3) (2023) 275–293, http://dx.doi.org/10.55730/1300-0985.1844.

[19] R.J. Walters, B. Parsons, T.J. Wright, Constraining crustal velocity fields with InSAR for Eastern Turkey: Limits to the block-like behavior of Eastern Anatolia, J. Geophys. Res.: Solid Earth 119 (6) (2014) 5215–5234, http://dx.doi.org/10.1002/2013JB010909.

[20] B. Aktuğ, H. Özener, A. Doğru, A. Sabuncu, B. Turgut, K. Halicioğlu, O. Yılmaz, E. Havazlı, Slip rates and seismic potential on the East Anatolian Fault System using an improved GPS velocity field, J. Geodyn. 94 (2016) 1–12, http://dx.doi.org/10.1016/j.jog.2016.01.001.

[21] R. Reilinger, S. McClusky, P. Vernant, S. Lawrence, S. Ergintav, R. Çakmak, H. Özener, F. Kadirov, I. Guliev, R. Stepanyan, M. Nadariya, GPS constraints on continental deformation in the Africa–Arabia–Eurasia continental collision zone and implications for the dynamics of plate interactions, J. Geophys. Res.: Solid Earth 111 (B5) (2006) http://dx.doi.org/10.1029/2005JB004051.

[22] E. Hussain, S. Kalaycıoğlu, C.W. Milliner, Z. Çakir, Preconditioning the 2023 Kahramanmaraş (Türkiye) earthquake disaster, Nat. Rev. Earth Environ. 4 (5) (2023) 287–289, http://dx.doi.org/10.1038/s43017-023-00411-2.

[23] CDP, 2023 Turkey-Syria earthquake, 2023, https://disasterphilanthropy.org/disasters/2023-turkey-syria-earthquake/. (Accessed 25 March 2025).

[24] UNOCHA, Humanitarian transition overview – Türkiye earthquake response, 2023, https://www.unocha.org/publications/report/turkiye/humanitarian-transition-overview-turkiye-earthquake-response-august-2023. (Accessed 10 January 2025).

[25] O. Tan, Long-term aftershock properties of the catastrophic 6 February 2023 Kahramanmaraş (Türkiye) earthquake sequence, Acta Geophys. (2024) 1–18, http://dx.doi.org/10.1007/s11600-024-01419-y.

[26] UNDP, Türkiye-Syria earthquakes, 2023, https://www.undp.org/turkiye-syria-earthquakes. (Accessed 25 March 2025).

[27] T. Kobayashi, H. Munekane, M. Kuwahara, H. Furui, Insights on the 2023 Kahramanmaraş Earthquake, Turkey, from InSAR: Fault locations, rupture styles and induced deformation, Geophys. J. Int. 236 (2) (2024) 1068–1088, http://dx.doi.org/10.1093/gji/ggad464.

[28] A. Dahal, H. Tanyaş, A.L. Handwerger, L. Lombardo, E. Fielding, Do earthquakes wake more slopes than they calm?, 2025, http://dx.doi.org/10.48550/arXiv.2508.08819.

[29] E. Damcı, R. Temür, Z. Kanbir, Ç. Şekerci, E.Ö. Köroğlu, Comprehensive investigation of damage due to 2023 kahramanmaraş earthquakes in Türkiye: Causes, consequences, and mitigation, J. Build. Eng. 99 (2025) 111420, http://dx.doi.org/10.1016/j.jobe.2024.111420.

[30] E. Mills, K. Smith, A. Winson, L. Bateson, R. Ciurean, Assessing sustained high-heat multi-hazard events through earth observation and impact chain analysis in southeast UK, IScience (2026) http://dx.doi.org/10.1016/j.isci.2026.115423.

[31] M. Zebisch, S. Terzi, M. Pittore, K. Renner, S. Schneiderbauer, Climate impact chains – A conceptual modelling approach for climate risk assessment in the context of adaptation planning, in: C. Kondrup, et al. (Eds.), Climate Adaptation Modelling, in: Springer Climate, Springer, Cham, 2022, http://dx.doi.org/10.1007/978-3-030-86211-4_25.

[32] L. Menk, S. Terzi, M. Zebich, E. Rome, D. Lückerath, K. Milde, S. Kienberger, Climate change impact chains: A review of applications, challenges, and opportunities for climate risk and vulnerability assessments, Weather. Clim. Soc. 14 (2) (2022) 619–636, http://dx.doi.org/10.1175/WCAS-D-21-0014.1.

[33] US Geological Survey (USGS), Field photographs of landslides triggered by the february 2023 kahramanmaraş, Türkiye earthquake sequence, 2023, http://dx.doi.org/10.5066/P1NFMKWL.
[34] M. Taftsoglou, S. Valkaniotis, G. Papathanassiou, E. Karantanellis, Satellite imagery for rapid detection of liquefaction surface manifestations: The case study of Türkiye–Syria 2023 earthquakes, Remote. Sens. 15 (17) (2023) 4190, http://dx.doi.org/10.3390/rs15174190.
[35] G. Tonuk, O. Cinicioglu, N. Milev, S. Torisu, T. Kiyota, T. Tobita, Geotechnical damages observed in the 2023 Turkey-Syria earthquake, in: Japanese Geotechnical Society Special Publication, Vol. 10, 2024, pp. 1659–1664, http://dx.doi.org/10.3208/jgssp.v10.OS-33-05.
[36] M. Heidarzadeh, A.R. Gusman, I.E. Mulia, The landslide source of the eastern Mediterranean tsunami on 6 February 2023 following the Mw 7.8 Kahramanmaraş (Türkiye) inland earthquake, Geosci. Lett. 10 (1) (2023) 1–16, http://dx.doi.org/10.1186/s40562-023-00304-8.
[37] R. Ferrell, Turkey, building codes, and the importance of regulation, 2023, https://www1.wsrb.com/blog/turkey-building-codes-and-the-importance-of-regulation. (Accessed 25 March 2025).
[38] A. Tilloy, B.D. Malamud, H. Winter, A. Joly-Laugel, A review of quantification methodologies for multi-hazard interrelationships, Earth-Sci. Rev. 196 (2019) 102881, http://dx.doi.org/10.1016/j.earscirev.2019.102881.
[39] T. Opitz, F. Bonneu, E. Gabriel, Point-process based Bayesian modeling of space–time structures of forest fire occurrences in mediterranean France, Spat. Stat. 40 (2020) 100429, http://dx.doi.org/10.1016/j.spasta.2020.100429.
[40] A. Dahal, R. Huser, L. Lombardo, At the junction between deep learning and statistics of extremes: Formalizing the landslide hazard definition, J. Geophys. Res.: Mach. Learn. Comput. 1 (3) (2024) e2024JH000164.
[41] K. He, Z. Fang, R. Zhang, S. Luo, S. Zhao, N. Liang, Joint modeling of co-seismic landslide occurrence and size with spatial dependence, Nat. Hazards 122 (1) (2026) 34, http://dx.doi.org/10.1007/s11069-025-07875-z.
[42] Ö. Kale, S. Akkar, A. Ansari, H. Hamzehloo, A ground-motion predictive model for Iran and Turkey for horizontal PGA, PGV, and 5% damped response spectrum: Investigation of possible regional effects, Bull. Seismol. Soc. Am. 105 (2A) (2015) 963–980, http://dx.doi.org/10.1785/0120140134.
[43] A. Özacar, E. Ayhan, B. Uzel, E. Sopacı, S. Shah, Z. Gülerce, N. Kaymakcı, H. Okay, B. Rojay, Complex active deformation along southwestern part of the East Anatolian Fault Zone: Insights from 2023 Türkiye earthquake doublet, 2025, http://dx.doi.org/10.5194/egusphere-egu25-9330.
[44] S.G. Wesnousky, Displacement and geometrical characteristics of earthquake surface ruptures: Issues and implications for seismic-hazard analysis and the process of earthquake rupture, Bull. Seismol. Soc. Am. 98 (4) (2008) 1609–1632, http://dx.doi.org/10.1785/0120070111.
[45] H.B. Okay, A.A. Özacar, A novel VS30 prediction strategy taking fluid saturation into account and a new VS30 model of Türkiye, Bull. Seismol. Soc. Am. 114 (2) (2023) 1048–1065, http://dx.doi.org/10.1785/0120230032.
[46] M. Alvioli, I. Marchesini, P. Reichenbach, M. Rossi, F. Ardizzone, F. Fiorucci, F. Guzzetti, Automatic delineation of geomorphological slope units with r.slopeunits v1.0 and their optimization for landslide susceptibility modelling, Geosci. Model. Dev. 9 (11) (2016) 3975–3991, http://dx.doi.org/10.5194/gmd-9-3975-2016.
[47] T. Hastie, R. Tibshirani, Generalized additive models: Some applications, J. Amer. Statist. Assoc. 82 (398) (1987) 371–386, http://dx.doi.org/10.1080/01621459.1987.10478440.
[48] T. Wang, K. Yin, Z. Wang, Z. Fang, A. Dahal, L. Lombardo, Long and short-term perspectives on space–time landslide modelling, Int. J. Appl. Earth Obs. Geoinf. 142 (2025) 104694, http://dx.doi.org/10.1016/j.jag.2025.104694.
[49] H. Tanyaş, K. Hill, L. Mahoney, I. Fadel, L. Lombardo, The world's second-largest, recorded landslide event: Lessons learnt from the landslides triggered during and after the 2018 Mw 7.5 Papua New Guinea earthquake, Eng. Geol. 297 (2022) 106504, http://dx.doi.org/10.1016/j.enggeo.2021.106504.
[50] E. Bryce, D. Castro-Camilo, C. Dashwood, et al., An updated landslide susceptibility model and a log-Gaussian Cox process extension for Scotland, Landslides 22 (2025) 517–535, http://dx.doi.org/10.1007/s10346-024-02368-9.
[51] D.W. Hosmer, S. Lemeshow, Applied Logistic Regression, second ed., John Wiley & Sons, New York, 2000, http://dx.doi.org/10.1002/0471722146.
[52] S. Brzev, C. Scawthorn, A.W. Charleson, L. Allen, M. Greene, K. Jaiswal, V. Silva, GEM Building Taxonomy (Version 2.0), Technical Report 2013–02, GEM Foundation, 2013.